Full Paper

Journal of the Brazilian Chemical Society

https://dx.doi.org/10.21577/0103-5053.20250148

J. Braz. Chem. Soc. **2025**, *36*, 11, e-20250148, 1-19

In silico Identification of Lanostane Triterpenes as GluN1-GluN2B NMDA Receptor Inhibitors

Jonatas M. Negreiro,[a] José A. C. Oliveira,[a] Fátima M. Nunes,[a] Francisco G. Barbosa,[a] Jair Mafezoli,[a] Marcos C. Mattos,[a] Danielle S. Macedo,[b] Geancarlo Zanatta[*,c] and Maria C. F. Oliveira*[*,a]

[a]*Departamento de Química Orgânica e Inorgânica, Centro de Ciências, Universidade Federal do Ceará, 60455-760 Fortaleza-CE, Brazil*

[b]*Núcleo de Pesquisa e Desenvolvimento de Medicamentos, Universidade Federal do Ceará, 60430-275 Fortaleza-CE, Brazil*

[c]*Departamento de Biofísica, Instituto de Biociências, Universidade Federal do Rio Grande do Sul, Laboratório 204, Prédio 43422, 91501-970 Porto Alegre-RS, Brazil*

N-Methyl-D-aspartate receptors (NMDARs) dysfunction can lead to impaired synaptic plasticity, learning and memory, and have been linked to various neuropsychiatric disorders, including cognitive dysfunction, schizophrenia, autism, epilepsy, and depression. NMDAR is a non-specific cation channel formed by different combinations of subunits, GluN1 and GluN2 family (A-D). Previous studies have indicated that the subunit GluN2B activity is linked to depressive symptoms. Herein, we utilize computational biology techniques to identify the inhibitory potential of lanostane triterpenes on the GluN1-GluN2B subunit of NMDARs. Ensemble-based virtual screening was performed to test 821 compounds against the crystallographic structure of GluN1-GluN2B. After physicochemical and pharmacokinetic analysis, compounds **55**, **59**, **61**, **75**, **77**, **80**, and **82** were found to have a favorable profile for developing potential drugs. Induced fitting simulations relaxed atomic contacts under solvated conditions, improving molecular interactions between the selected ligands and the NMDA. Binding free energy calculations corroborated the stability of the protein-ligand complexes, indicating that compounds **55**, **75**, and **82** are the most promising inhibitors. These findings demonstrate the potential of lanostane triterpenes as candidates for treating neuropsychiatric conditions associated with NMDA dysfunction, contributing to the search for new therapies that aim to selectively and effectively modulate the activity of this receptor.

Keywords: NMDA receptors, depression, GluN2B, lanostane triterpenes, ensemble docking, MM-GBSA

Introduction

N-Methyl-D-aspartate receptors (NMDARs) are involved in multiple physiological processes, including synaptic signaling, plasticity, growth, differentiation, apoptosis, and neural functions like learning, memory, and neurogenesis.[1] Specifically, NMDARs are essential for proper signal transmission in the brain, contributing to information propagation, cognition, and memory formation through their unique function in inducing long-term synaptic plasticity.[2] Additionally, NMDARs play a crucial role in uniquely regulating postsynaptic activities. Their activation requires both glutamate release and postsynaptic membrane depolarization, which results in calcium influx and the subsequent modulation of neuronal processes. Dysfunction of NMDARs can lead to impaired synaptic plasticity, learning, and memory, and have been associated with various neuropsychiatric disorders, including cognitive dysfunction, schizophrenia, autism, epilepsy, and depression.[3,4]

NMDAR antagonists comprise a pharmacological class characterized by a broad range of therapeutic uses. Specifically, ketamine, which acts as a noncompetitive antagonist at the NMDA receptor, has demonstrated effectiveness in the management of treatment-resistant depression (TRD). Notably, it induces rapid and sustained antidepressant effects following a limited number of

*e-mail: mcfo@ufc.br; geancarlo.zanatta@gmail.com
Editor handled this article: Paulo Augusto Netz (Associate)

doses.[5] TRD affects up to two-thirds of patients with depression, who experience symptom relapse or non-responsiveness to conventional antidepressant treatments targeting monoamine neurotransmitters, such as serotonin, dopamine, and norepinephrine.[6] Another noncompetitive NMDAR antagonist, memantine, is approved for managing moderate to severe Alzheimer's disease. This drug helps to stabilize cognitive decline by attenuating the neurotoxic effects associated with excessive glutamate release.[7] Beyond these, NMDAR antagonists are also explored for their potential to ameliorate symptoms of schizophrenia,[8] neuropathic pain,[9] and as adjuncts in anesthesia,[10] due to their neuroprotective properties. Therefore, anti-NMDA drugs hold promise for a range of future therapeutic applications.

While anti-NMDA therapies, such as ketamine, present promising therapeutic advantages, the prescription of these agents requires careful consideration given the spectrum of potential adverse effects, including dissociative experiences, hallucinations, elevations in heart rate and blood pressure, and bladder toxicity. To ascertain the safety profile associated with prolonged, routine administration, it is imperative that extensive clinical trials be undertaken. These trials should encompass a range of ketamine dosages and incorporate extended follow-up periods to thoroughly investigate the risks of cognitive impairment, as well as the potential for dependence and abuse.[11] Therefore, additional research is required to optimize the therapeutic window for existing anti-NMDA drugs and develop novel anti-NMDA drugs with a lower side effects profile. The proposed research directions include investigating novel NMDA receptor subunit-specific drugs[12] and alternative glutamatergic targets that provide greater treatment specificity.

NMDARs are heterotetrametric complexes composed of various subunits, typically including GluN1, and GluN2 (A-D). GluN2B, plays a crucial role in the development of depression.[12] In this regard, studies have indicated that GluN2B activity is linked to depressive-like behaviors induced by prenatal stress, with elevated glutamate levels in the hippocampus of susceptible offspring.[13] Additionally, the blockade of GluN2B subunits has demonstrated rapid-acting antidepressant-like effects independent of serotonin reuptake inhibition, highlighting the potential of GluN2B as a target for pharmacotherapies in depression.[5]

The need for effective and safe medications to treat depression led to the study of natural products with antidepressant properties.[14] In this regard, there are various classes of natural products with antidepressant properties, such as flavonoids,[15,16] polyphenols,[17] alkaloids,[18] essential oils,[19] and terpenoids.[20] Among these, terpenoids represent the largest and most diversified group of naturally occurring organic compounds and are highlighted for their therapeutic potential against neurodegenerative diseases.[21,22]

With widespread distribution in traditional Chinese medicines, over 20,000 triterpenes have been isolated and identified in nature, and they are classified into different groups according to the basic skeleton. Lanostane-type triterpenes have 30 or 27 carbon atoms, although structures with 24 atoms have also been found. The basic skeleton (Figure 1) of this type of triterpene shows *trans* configuration between rings A/B, B/C, and C/D, besides C-10β, C-13β, C-14α and C-17β substituents. In addition to these characteristics, representatives of this group also contain substituents at positions C-3, 7, 11, 12, 15, 22, 23, 24, and 25 of the parental nuclei.[23]

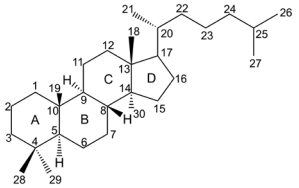

Figure 1. Skeletal structure of lanostane-type triterpenes.

The study carried out by Ruszkowski *et al.*[24] demonstrated that triterpenoids and semisynthetic analogs exhibit activity against neurodegenerative diseases. Additionally, lanostane-type triterpenes from the fungus *Ganoderma lucidum* exhibited potential therapeutic effects as antineuroinflammatory, antioxidant, and cytoprotective agents.[23] While these broad activities are beneficial, a more direct mechanistic link justifies their investigation as modulators of the glutamatergic system. A central pathological mechanism underlying depression and neurodegeneration is glutamate-induced excitotoxicity, which is primarily mediated by the overactivation of NMDA receptors.[25] Crucially, recent studies provide direct evidence supporting this link, showing that lanostane triterpenoids from *Ganoderma* species offer potent protection against glutamate-induced cytotoxicity in both *in vitro* and *in vivo* models by mitigating oxidative stress.[26] Similarly, other triterpenoids have been shown to protect primary cortical cells from glutamate-induced damage, suggesting a direct interaction with the glutamatergic system.[22] The well-documented anti-neuroinflammatory activity of lanostane triterpenes provides another strong rationale for this hypothesis, as neuroinflammation and excitotoxicity are known to be deeply intertwined pathological processes.

Reinforcing the broad therapeutic interest in this class of natural products, our research group has recently investigated the anti-myelocytomatosis (anti-MYC) potential of lanostane-type triterpenes through a comprehensive *in silico* approach similar to the one employed in the present

study, identifying promising candidates for anticancer therapy.[27] These collective findings highlight the versatility of lanostane triterpenes as privileged scaffolds for drug discovery and form the basis of our hypothesis.

Here, using a combination of computational methods (absorption, distribution, metabolism, elimination and toxicity (ADMET), Ensemble Docking, Induced Fitting, and Molecular Mechanics Generalized-Born Surface Area (MM-GBSA)), we tested the hypothesis that lanostane-type triterpenes could serve as inhibitors of the GluN1-GluN2B subunits of NMDA receptors, potentially representing novel candidates for fast-acting antidepressant drugs.

Methodology

Structural data

In this study, the crystallographic structure of NMDA receptor (PDB ID: 5EWJ), solved at 2.77 Å of resolution, and comprising of the amino-terminal domains GluN1 and GluN2B in complex with ifenprodil was used.[28] Missing atoms were modeled using the SWISS-MODEL web server.[29-31] During modelling, the crystallographic coordinates were used as a template, while the primary sequence (ID: A0A1L8F5J9) was retrieved from the Uniprot server.[32,33] The final model was analyzed using the Ramachandran plot, generated through the ProCheck webserver,[34,35] prior to the protonation at pH 7.4 using the PROPKA code, available on the PDB2PQR[36,37] web server.

At total, 821 lanostane-type triterpenes were chosen based on information from scientific publications, following the (*R*) or (*S*) stereochemistry of the lanostane-type triterpene structures as described in the original literature. The chemical representations of each compound, at pH 7.4, were obtained by modeling the planar (2D) with ChemDraw Ultra 12.0 software,[38] following by energy minimization steps, using the MMFF94 force field available in the Avogadro program (version 1.2), to obtain three-dimensional (3D) structures.[39]

Analysis of the structural diversity of the 821 investigated lanostane triterpenes allowed us to separate them into the following skeletons (I-XXII) depicted at Figure 2: saturated (I), 7(8)-ene (II), 8(9)-ene (III), 9(11)-ene (IV), 13(17)-ene (V), 8(14)-ene (VI), 8(9)-ene lactone (VII), 7(8),9(11)-diene (VIII), 7(8),12(13)-diene (IX), 7(8),14(15)-diene (X), 8(9),16(17)-diene (XI), 9(11),16(17)-diene (XII), 1(2),7(8),9(11)-triene (XIII), *seco*-8-ene (XIV), 3,4-*seco*-8(9)-diene (XV), 3,4-*seco*-9(11)-diene (XVI), 3,4-*seco*-7(8),9(11)-triene (XVII), rearranged 7(8)-ene lactone (XVIII), rearranged 9(11)-ene

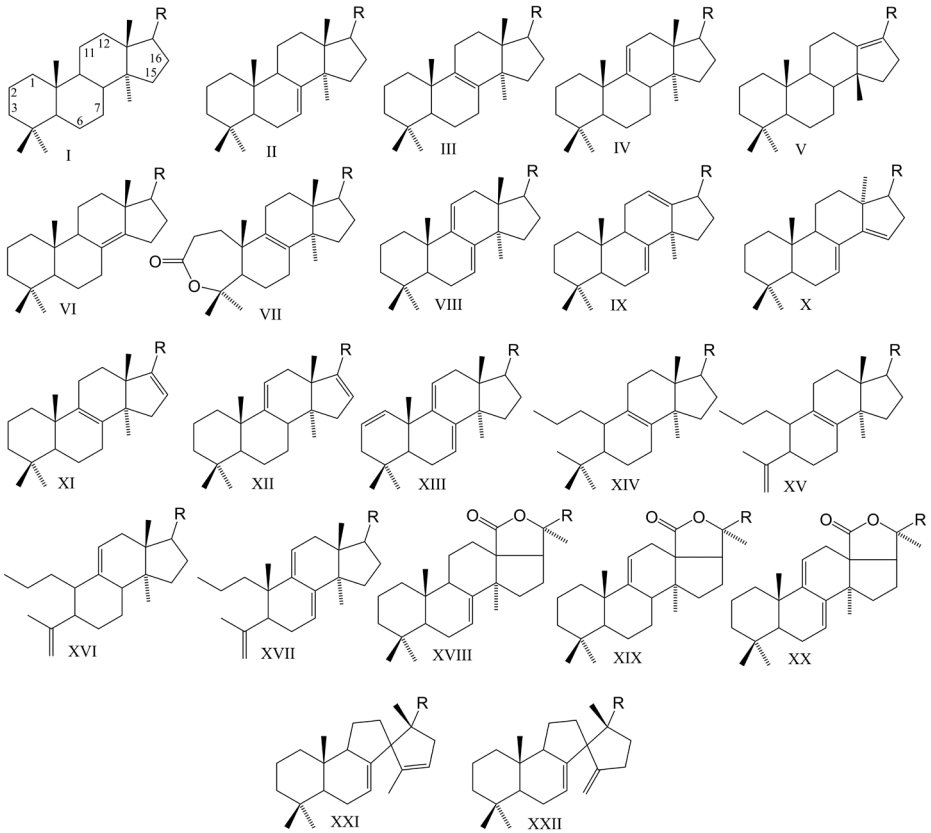

Figure 2. Main carbon skeletons (I-XXII) of the 821 lanostane triterpenes identified in the compound library.

lactone (XIX), rearranged 7(8),9(11)-diene lactone (XX), rearranged 7(8),14(15)-diene (XXI), and rearranged 7(8),14(30)-diene (XXII). In general, the side chain (*R*) at C-17 is highly diverse, and oxygenated organic functions such as alcohol, ether, ester, ketone, aldehyde, and carboxylic acid are commonly present at positions 1, 2, 3, 6, 7, 11, 12, 15, and 16.

Ensemble generation

Molecular sampling was performed through molecular dynamics simulations using GROMACS v.2019 package[40] with the AMBER99SB force field.[41] To capture the intrinsic flexibility of the receptor, the crystallographic ligand (ifenprodil) was removed, and the resulting *apo* protein was used for the simulation. This system was then inserted in a cubic box with volume of 437 nm^3, and the TIP3P water model was employed to describe water molecules. Net charge was neutralized by adding Na^+ and Cl^- ions at 0.15 mol L^{-1} concentration. Energy minimization was performed using steepest algorithm. The system was balanced by gradually decreasing constraint forces over 4 steps of 1,000 ps each. The long-range electrostatic interaction calculation was modeled with the Particle Mesh Ewald (PME) method. Temperature coupling was performed using the V-rescale thermostat method set to 303.15 K and Berendsen barostat with a reference pressure at 1 atm. The LINCS algorithm was used to constrain the covalent bonds to their equilibrium length. The root-mean-square deviation (RMSD) of the backbone atoms was employed to track molecular fluctuations during the production step. The resulting 300-ns trajectory was used as input in the EnGens pipeline,[42] aiming for the identification and clustering of conformational states visited by the complex during the sampling procedure. The clustering analysis was centered at residues Tyr109A, Leu135A, Pro78B, Ala107B, Gln110B, Ile111B, Thr174B, Phe176B and Glu236B, which make up the binding site.[43] Following, featurization was performed using the backbone torsions and the minimum distance between all pairs of residues. The standard principal component analysis (PCA) method, with a variation threshold set at 85%, was employed for dimensionality reduction, and the K-means method was employed for clustering, using the silhouette method to estimate the appropriate number of clusters. At the end, a conformational ensemble, to be used during the docking procedure, was obtained by extracting one representative member from each cluster.

Ensemble-based virtual screening

Initially, to set the docking protocol, AutoDock Vina 1.2 software[44] was used to dock the modeled protein against ifenprodil (**1**) in the co-crystallized geometry (PDB ID: 5EWJ).[28,45] The search area was set to 17.5, 19, 19 (xyz), with center in 84.76, 6.0, –32.3 (xyz), to include the binding site amino acids Tyr109A, Leu135A, Pro78B, Ala107B, Gln110B, Ile111B, Thr174B, Phe176B and Glu236B. Following, an in-house ensemble docking protocol was employed to screen all 821 lanostane triterpene compounds against the selected binding pocket of the NMDA modeled protein.

Druglikeness prediction and pharmacokinetic parameters

Druglikeness prediction and pharmacokinetic parameters were performed through the web servers SwissADME[46,47] and ADMETlab 2.0.[48,49] SwissADME tool was employed to estimate druglikeness, distribution coefficient (Log $D^{7.4}$) and oral bioavailability according to Lipinski[50,51] and Veber[52] parameters. ADMETlab tool was employed to estimate parameters of absorption, distribution, metabolism, elimination and toxicity (ADMET). The properties analyzed for screening were as follows: P-glycoprotein inhibitor (Pgpi), P-glycoprotein substrate (Pgps), probability of overcoming the blood-brain barrier (BBB) and hERG channel blocker (hERG), along with assessments for hepatotoxicity and mutagenicity, based on Drug Induced Liver Injury (DILI) and Ames Mutagenicity Assay (AMES) values.

Induced fitting on docking results

To relax the geometry of the system and correct improper geometries obtained during docking procedures, resulting complexes were submitted to molecular dynamics simulations using GROMACS v.2019 package[40] with the AMBER99SB[41] force field. Each system was inserted in a cubic box with volume of 437 nm^3, and the TIP3P water model was employed to describe water molecules. Systems were solvated using 41938 water molecules, under periodic boundary conditions. Net charge was neutralized by adding Na^+ and Cl^- ions at 0.15 mol L^{-1} concentration. Energy minimization was performed using steepest algorithm. The system was balanced by gradually decreasing constraint forces over 4 steps of 1,000 ps each. The long-range electrostatic interaction calculation was modeled with the Particle Mesh Ewald (PME) method. Temperature coupling employed the V-rescale thermostat set to 303.15 K and the Berendsen barostat was employed to set a reference pressure at 1 atm. The LINCS algorithm was used to constrain the covalent bonds to their equilibrium length. The root-mean-square deviation (RMSD) of the backbone

atoms was employed to monitor the fluctuations of the complex. At total, a 400 ns trajectory for each complex was obtained during the production step. Molecular interactions and geometry fluctuations were analyzed using the GROMACS tools rmsf, rms, and hbond.

Binding free energy calculations

Following the induced fitting simulations, each receptor-ligand complex was submitted to binding free energy calculations through the Molecular Mechanics Generalized-Born Surface Area (MM-GBSA) method, available in the gmx_MMPBSA code.[53] Calculations were performed by sampling 100 frames from the last 10 ns of each trajectory (390-400 ns). A set of calculations were performed by setting the protein dielectric constant to 2 and solvent dielectric constant to 20, 40 or 80. The generalized Born Method parameter "igb" was set to 2; the energy decomposition scheme "idecomp" set to 2; and the verbosity level output "dec_verbose" was set to 3. To ensure a comprehensive analysis, the ligand and all residues located within 10.0 Å from the ligand were used to calculate the binding energy. Temperature was set to 303.15 K and the salt concentration to 0.15 mol L^{-1}. The binding free energy was calculated as the difference between the free energies of the complex and the isolated components (receptor or ligand). Therefore, the binding free energies of each component (complex, receptor and ligand) was obtained according to equation 1.

$$\Delta G_{bind} = \Delta G_{complex} - (\Delta G_{receptor} + \Delta G_{ligand}) \quad (1)$$

In this equation 1, $\Delta G_{complex}$, $\Delta G_{receptor}$ and ΔG_{ligand} represent the free energies of the complex, the receptor and the ligand, respectively. The binding free energy can be decomposed into enthalpic (ΔH) and entropic (ΔS) terms by equation 2:

$$\Delta G_{bind} = \Delta H - T\Delta S \quad (2)$$

where $\Delta H = \Delta E_{MM} + \Delta G_{solv}$ is the bond enthalpy.

The individual free energy[54] of each term ($\Delta G_{complex}$, $\Delta G_{protein}$ and ΔG_{ligand}) can be calculated using equation 3:

$$\Delta G = \Delta E_{MM} + \Delta G_{solv} - TS \quad (3)$$

where E_{MM} is the mechanical-molecular energy in vacuum, G_{solv} is the solvation energy, T is the temperature and S is the entropy. Mechanical-molecular energy can be decomposed into different energetic components by equation 4:

$$\Delta E_{MM} = \Delta E_{elec} + \Delta E_{vdw} \quad (4)$$

where, ΔE_{elec} and ΔE_{vdw} are the electrostatic and van der Waals energies, respectively.

Solvation energy can be decomposed into polar and non-polar components by equation 5:

$$\Delta G_{solv} = \Delta G_{GB} + G_{SURF} \quad (5)$$

The polar solvation energy was calculated using the GB method. Energy decomposition analysis was carried out *per* residue to verify those residues that contributed the most to the receptor-ligand interactions.

Results and Discussion

The investigation of the neuroprotective potential of 821 lanostane-type triterpenes involved computational techniques and was developed according to the workflow displayed in Figure 3.

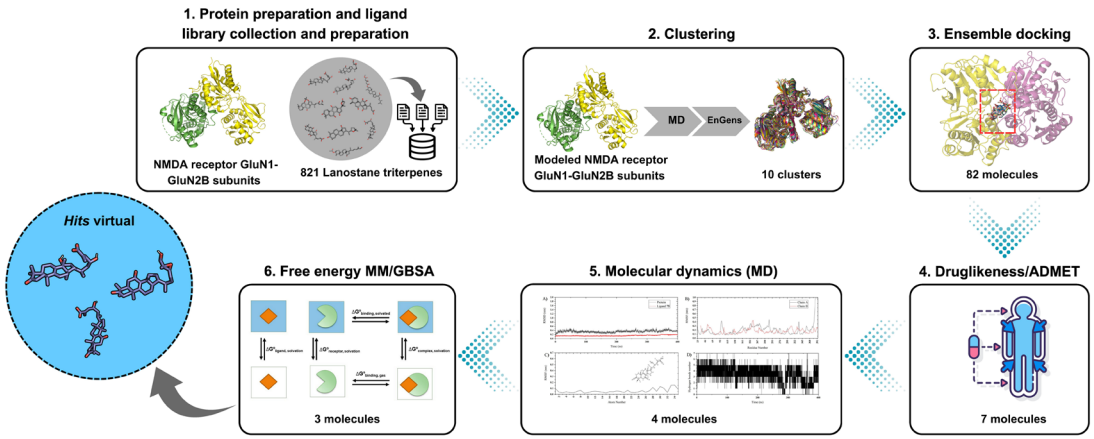

Figure 3. Computational workflow used in this study. The pipeline includes molecular modeling of the NMDA receptor GluN1-GluN2B subunits, conformational sampling via molecular dynamics (MD), ensemble clustering with EnGens, ensemble docking of 821 lanostane-type triterpenes, ADMET-based filtering, induced fit MD simulations of selected ligands, and MM-GBSA binding free energy calculations.

NMDA receptor modeling

The NMDA receptor was constructed using homology modeling via the SWISS-MODEL web server.[29-31] The protein sequence was retrieved from the UniProt server (A0A1L8F5J9), while the structural coordinates PDB ID: 5EWJ were used as a template. Sequence alignment using the ClustalW program showed 99.15% identity between the model and the input sequence. It is worth mentioning that reliable models present 30% or more identity.[55]

The constructed model was evaluated using the Ramachandran graph (Figure S1, Supplementary Information (SI) section), which showed that 90.7% of residues are in favored regions, 9.3% are in additional allowed regions, and no amino acids were found in regions not allowed.

Conformational ensemble

The EnGens pipeline, developed by Conev *et al.*,[42] was used to generate the conformational ensemble. This automated pipeline can generate and analyze conformational ensembles of molecular targets, and its operation is simplified by providing an ensemble of data structural proteins as input. In the present study, the input to EnGens was an ensemble of dynamic protein data from molecular dynamics (MD) simulations.

A 300 (ns) trajectory, obtained through MD simulations with the AMBER99SB force field, was employed to obtain a representative set of conformations that reflected the structural states of the molecular target. The system was considered to have reached equilibrium for conformational selection once the backbone root-mean-square deviation (RMSD) plateaued, exhibiting stable fluctuations around an average value (typically < 2 nm)[56] for the remainder of the simulation, as shown in Figure S2 (SI section). After obtaining the relaxed protein through this process, the resulting trajectory was used as an input file in the EnGens pipeline.

Processing the MD trajectory by EnGens generated a set of ten clusters of representative conformations, as shown in Figure 4a. In this representation, the y-axis represents the proportion of belonging to each cluster (cluster weight), while the x-axis displays the indices corresponding to the clusters. Figure 4b presents silhouette analysis, which is a measure of how well the points within each cluster are grouped. The red dotted line shows the average value of the silhouette coefficient for all clusters. In this case, the average value is 0.10980076, which indicates reasonable clustering. The points are colored according to their respective clusters.

Ensemble docking

Before performing the ensemble docking simulations with the 821 selected compounds, self-docking was performed with the AutoDock Vina 1.2 software[44] of the modeled protein against the cocrystallized ligand extracted from PDB ID: 5EWJ, the drug ifenprodil (**1**),[28,45] an antagonist with proven efficacy at the NMDA receptor GluN1-GluN2B subunits. This molecular docking aimed to identify essential receptor-ligand interactions. The investigation conducted by Singh *et al.*[43] elucidated that residues Tyr109A, Leu135A, Pro78B, Ala107B, Gln110B, Ile111B, Thr174B, Phe176B, and Glu236B play a key role in mediating the receptor-ligand interaction. Thus, these residues were designated as essential reference points to delineate the dimensions of the simulation box during the molecular self-docking procedures. To validate the computational conditions, the RMSD was calculated between the cocrystallized and docked ligand **1**,

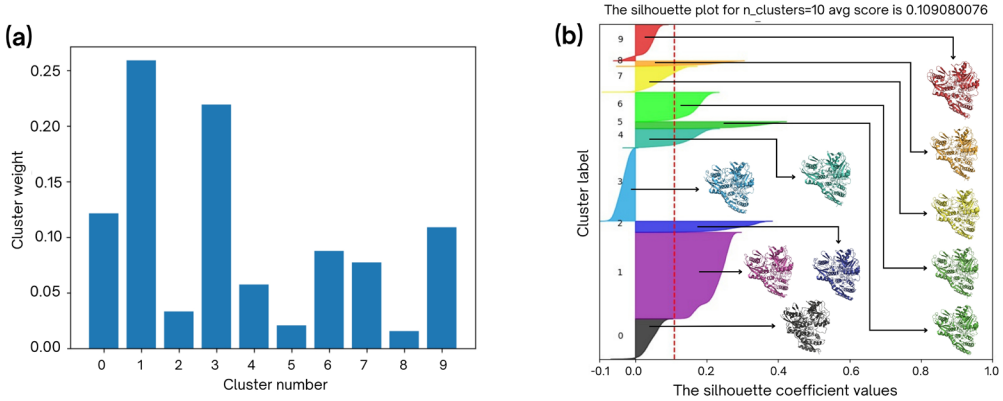

Figure 4. Clustering of target protein conformations by the EnGens pipeline. (a) Weights of the clusters obtained from the MD trajectory. (b) Silhouette coefficients of the clusters and their corresponding representative structure. The red dotted line shows the average value of the silhouette coefficient, which is 0.10980076.

indicating a value of 0.3019 Å and a binding energy value of −11.200 kcal mol^{-1} (as presented in Table 1). Therefore, the computational technique proved to be valid. The main amino acid residues that interact with the cocrystallized ligand **1** during the molecular docking step are Pro78B, Gln110B, Ile111B, Phe114B, Leu135A, Phe176B, and Pro177B, as shown in Figure S3 (SI section).

Ensemble docking simulations were conducted using the ten clusters previously generated by the EnGens pipeline, juxtaposed against a library of 821 lanostane triterpene ligands. Each resulting receptor-ligand assembly was thoroughly analyzed and classified based on the lowest interaction energies. In this way, 82 ligands (**2-83**) were selected, representing approximately 10% of the complexes with the best interaction energy (from −17.511 to −10.915 kcal mol^{-1}). The calculated interaction energies of the complexes, including the one involving the drug ifenprodil (ligand **1**), are listed in Table 1.

Table 1. Binding energies from ensemble docking for the 83 complexes, including ifenprodil (ligand **1**), ranked according to their interaction energy with different conformational clusters of the NMDA receptor

Ligand	Cluster	Binding energy / (kcal mol^{-1})	Binding energy ratio (*vs*. ifenprodil)	Ligand	Cluster	Binding energy / (kcal mol^{-1})	Binding energy ratio (*vs*. ifenprodil)
1	–	−11.200	1.000	**43**	9	−11.407	1.018
2	2	−17.511	1.563	**44**	9	−11.398	1.018
3	9	−15.859	1.416	**45**	9	−11.364	1.015
4	0	−15.111	1.349	**46**	9	−11.356	1.014
5	9	−14.579	1.302	**47**	9	−11.345	1.013
6	6	−14.143	1.263	**48**	9	−11.334	1.012
7	9	−13.883	1.240	**49**	9	−11.326	1.011
8	9	−13.870	1.238	**50**	9	−11.302	1.009
9	8	−13.771	1.230	**51**	8	−11.288	1.008
10	9	−13.759	1.228	**52**	9	−11.268	1.006
11	9	−13.560	1.211	**53**	9	−11.246	1.004
12	1	−13.263	1.184	**54**	9	−11.241	1.004
13	6	−13.069	1.167	**55**	9	−11.238	1.003
14	9	−12.819	1.145	**56**	8	−11.228	1.003
15	5	−12.774	1.141	**57**	9	−11.212	1.001
16	9	−12.741	1.138	**58**	9	−11.199	1.000
17	9	−12.484	1.115	**59**	9	−11.192	0.999
18	9	−12.393	1.107	**60**	0	−11.191	0.999
19	9	−12.266	1.095	**61**	9	−11.189	0.999
20	9	−12.248	1.094	**62**	3	−11.167	0.997
21	9	−12.225	1.092	**63**	6	−11.160	0.996
22	9	−12.103	1.081	**64**	9	−11.158	0.996
23	0	−11.941	1.066	**65**	9	−11.131	0.994
24	9	−11.916	1.064	**66**	9	−11.127	0.993
25	9	−11.905	1.063	**67**	9	−11.123	0.993
26	9	−11.904	1.063	**68**	9	−11.116	0.993
27	9	−11.850	1.058	**69**	9	−11.113	0.992
28	9	−11.717	1.046	**70**	9	−11.111	0.992
29	9	−11.705	1.045	**71**	9	−11.060	0.988
30	9	−11.692	1.044	**72**	6	−10.994	0.982
31	9	−11.648	1.040	**73**	9	−10.983	0.981
32	9	−11.646	1.040	**74**	5	−10.982	0.981
33	9	−11.602	1.036	**75**	9	−10.982	0.981
34	2	−11.564	1.033	**76**	9	−10.973	0.980
35	9	−11.519	1.028	**77**	9	−10.966	0.979
36	9	−11.516	1.028	**78**	9	−10.964	0.979
37	2	−11.511	1.028	**79**	6	−10.963	0.979
38	6	−11.501	1.027	**80**	2	−10.948	0.978
39	9	−11.486	1.026	**81**	9	−10.937	0.977
40	9	−11.476	1.025	**82**	9	−10.915	0.975
41	9	−11.438	1.021	**83**	9	−10.915	0.975
42	9	−11.417	1.019				

Additionally, the binding energy ratio relative to ifenprodil (–11.200 kcal mol^{-1}) is also displayed to facilitate a direct comparison of the predicted affinities. The 2D structures of these compounds are represented in Table S1 (SI section). The 82 selected ligands were used to predict druglikeness and pharmacokinetic properties.

Physicochemical and pharmacokinetic properties

The *in silico* study of the physicochemical and pharmacokinetic properties of ifenprodil ligand (**1**) and the 82 ligands (**2-83**) was done using SwissADME web servers[46,47] and ADMETlab 2.0.[48,49] The results for the 82 selected ligands can be seen in Tables S2 and S3 (SI section).

The Lipinski[50,51] and Veber[52] rules are widely used in drug development to assess the druglikeness of molecules, i.e., the probability of a molecule being bioactive and viable as an oral drug. Lipinski's rules include four main criteria: molecular weight (MW), which should be no greater than 500 daltons; cLogP values between 1 and 5, selected for their potential to act on the central nervous system; the number of hydrogen bond donors (HBD), which should not be greater than 5, and the number of hydrogen bond acceptors (HBA), which should not be greater than 10. These properties have been observed in most oral drugs with these physicochemical characteristics, which favor intestinal absorption. Veber's rule aims to improve the ability to predict the oral bioavailability of compounds. To this end, it should be noted that the number of rotatable bonds (NRB) should not be greater than 10. Rotatable bonds are a measure of the flexibility of the molecule, which can affect its ability to cross cell membranes. Another property involved is the polar surface area (TPSA - topological polar surface area), which should not exceed 140 $Å^2$ (Ångstroms squared).

In the central nervous system (CNS), the blood-brain barrier (BBB) serves as a pivotal defense mechanism. Comprising a highly selective, semipermeable membrane, the BBB safeguards the CNS by preventing the ingress of potentially deleterious substances and pathogens present in the systemic circulation. Despite its protective role, the BBB concurrently imposes a significant challenge by impeding the penetration of numerous therapeutically beneficial drugs into the brain tissue. For the advancement of drug development targeting neuropsychiatric disorders, the selection of compounds with robust CNS penetration capabilities is crucial.[57] Cardiotoxic effects related to hERG (human ether-a-go-go-related gene) are also an important feature, since testing a new molecule for hERG safety is a mandatory requirement by the US FDA (United States Food and Drug Administration). Drug development should be monitored to see if it causes hERG channel blockade, since this channel is expressed in the brain and heart and has a central role in mediating the repolarization of action potentials.[58]

Another criterion is low hepatotoxicity and mutagenicity based on DILI (Drug-Induced Liver Injury) and AMES (Ames Mutagenicity Assay) values provided by the ADMETlab 2.0 software. This latter is a useful *in silico* tool for predicting ADMET-related properties. The DILI test can forecast the hepatotoxic potential of a drug candidate molecule using *in vitro* or *in vivo* models.[59] The AMES toxicity test predicts the ability of a substance to cause deoxyribonucleic acid (DNA) mutations using bacteria as a detection system. The result of this test can predict the carcinogenic potential of a drug candidate since mutation is often involved in carcinogenesis.[60] P-glycoprotein (P-gp), a multidrug transporter, plays a key role in regulating ADMET properties by significantly influencing the absorption, distribution, metabolism, and elimination of drugs and toxins. Functioning as a transmembrane glycoprotein, P-gp uses the energy of adenosine triphosphate (ATP) to expel several lipophilic molecules from the cell, protecting it against toxic substances and maintaining cellular homeostasis.[61] P-Glycoprotein selectively removes certain endogenous and exogenous molecules from the brain's circulation, thereby regulating the BBB function. Recent research[62] indicates that P-gp may impede the uptake of several antidepressants, which could explain the low effectiveness of conventional antidepressant treatments.

Based on the properties discussed above, the lanostane-type triterpene compounds were selected according to the following filter: the compounds must follow the Lipinski and Veber rules with MW ≤ 500 daltons; cLogP ≤ 5; HBD ≤ 5; HBA ≤ 10; NRB ≤ 10 and TPSA ≤ 140 $Å^2$. Also use as criteria BBB > 50%, hERG < 50% (being classified as "Non-blocking"), low hepatotoxicity and mutagenicity, with DILI and AMES values < 50%, and the low probability of being a substrate for P-glycoprotein Pgps < 50% and being an inhibitor thereof (Table 2).

Analyzing Table 3, it can be observed that the selected triterpene ligands presented better results in terms of pharmacokinetic properties and toxic potential, with an hERG value of 82.80%, and therefore it is quite likely that they act as active blockers of the hERG channel. The BBB value was 57.40%, a lower value compared to the other selected triterpene ligands. In addition, ligand **1** presented Pgpi values of 0.70% and Pgps of 87.60%, indicating that it is probably a P-gp substrate and not an inhibitor. On the other hand, the triterpene compounds (**55**, **59**, **61**,

75, **77**, **80**, and **82**) presented opposite values, suggesting that they are not P-gp substrates, that is, that P-gp does not recognize them or actively transport them out of the cells.

After applying the filter, seven ligands were selected (Figure 5): **55**, **59**, **61**, **75**, **77**, **80**, and **82**, and the values of the physical-chemical properties and the pharmacokinetic parameters of the seven selected ligands, based on the filter used, can be seen in Tables 2 and 3, respectively.

The selected ligands were triterpenes with carbonyl, hydroxyl, carboxyl, and ester functional groups, highly oxygenated molecules with a strong propensity to act as hydrogen bond donors or acceptors. Most of these triterpenes have acidic groups in their side chains and are related to structural similarities, such as unsaturation in their main skeleton.

All the selected compounds are natural products produced by fungus species from *Ganoderma* genus. Ligand **55** (epoxyganoderiol A) was isolated from *G. lucidum*,[63] while ligands **59** (ganohainanic acid D) and **75** (hainanic acid A) were isolated from *G. hainanense.*[64] Ligand **61** (ganodeweberiol C), isolated from the fruiting bodies of *G. weberianum*, was active against the HeLa cell line with an half-maximal inhibitory concentration (IC_{50}) value of 17.0.[65] Ligand **77** (*N*-lucidenic acid) was isolated from the dried fruiting bodies of *G. lucidum* and

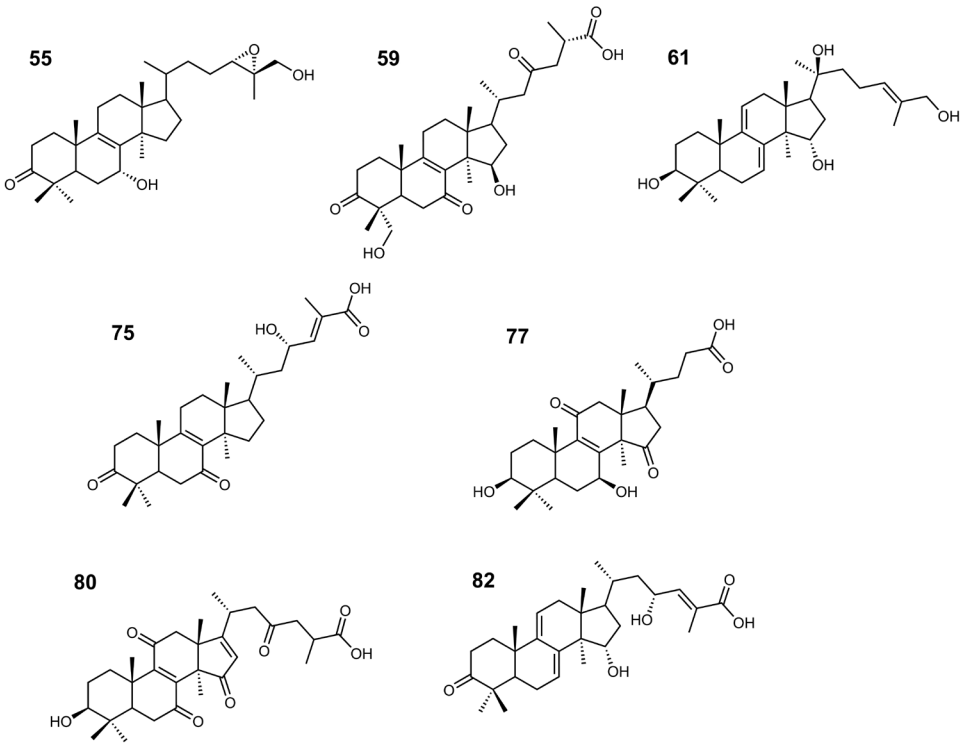

Figure 5. 2D structures of the selected set: **55**, **59**, **61**, **75**, **77**, **80**, and **82**, which were selected based on ensemble docking, physical-chemical properties and the pharmacokinetic parameters.

Table 2. Physicochemical properties (drug-likeness) of ligands **55**, **59**, **61**, **75**, **77**, **80**, and **82** that comply with Lipinski's and Veber's rules, in comparison with ifenprodil (**1**)

Selected compounds	MW / Da	cLogP	HBD	HBA	NRB	TPSA / Å^2
1	325.440	3.41	2	3	5	43.70
55	472.700	4.16	2	4	5	70.10
59	516.670	1.77	3	7	7	129.00
61	458.670	3.59	4	4	5	80.90
75	484.670	3.64	2	5	5	91.70
77	460.600	3.17	3	6	4	112.00
80	512.630	2.69	2	7	6	126.00
82	484.670	3.31	3	5	5	94.80

MW: molecular weight; cLog P: partition coefficient; HBD: hydrogen bond donors; HBA: hydrogen bond acceptors; NRB: number of rotatable bonds; TPSA: topological polar surface area.

Table 3. Predicted pharmacokinetic properties and toxicological profiles of the hERG[a] non-blocker compounds **55**, **59**, **61**, **75**, **77**, **80**, and **82**, in comparison with ifenprodil (**1**)

Selected compounds	BBB[b] / %	DILI[c] / %	AMES toxicity[d] / %	Pgpi[e] / %	Pgps[f] / %
1	57.40	1.00	1.60	0.70	87.60
55	66.70	6.50	3.40	97.00	0.20
59	93.30	5.60	1.60	83.50	0.80
61	93.80	0.40	0.50	99.60	3.60
75	92.80	10.40	1.70	43.00	0.00
77	92.50	3.90	0.80	55.80	3.80
80	97.70	16.30	1.80	89.40	0.70
82	98.60	2.50	0.60	71.90	0.70

[a]hERG channel blocker (hERG); [b]probability of crossing the blood-brain barrier (BBB); [c]drug-induced liver injury (DILI); [d]ames mutagenicity assay (AMES toxicity); [e]P-glycoprotein inhibitor (Pgpi); [f]P-glycoprotein substrate (Pgps).

showed significant cytotoxic activity against Hep G2, Hep G2,2,15 and P-388 tumor cells.[66] Ligand **80**, identified as 3β-hydroxy-7,11,15,23-tetraoxo-lanost-8,16-dien-26-oic acid, was previously isolated from the fruiting bodies of *G. theaecolum*.[67] Ligand **82** (ganoderic acid Jc), isolated from the fruiting bodies of *G. sinense*, showed selective inhibitory activity against HL-60 cells (IC_{50} = 8.30 μM).[68]

Receptor-ligand interactions

The receptor-ligand interaction was studied with the seven ligands selected (Figure 5). Figure 6 shows the interactions involved during the molecular coupling of the ligands, where the hydrogen bond interactions are highlighted with a dotted line in yellow. It is observed that ligand **55** has only one hydrogen bond interaction (residue

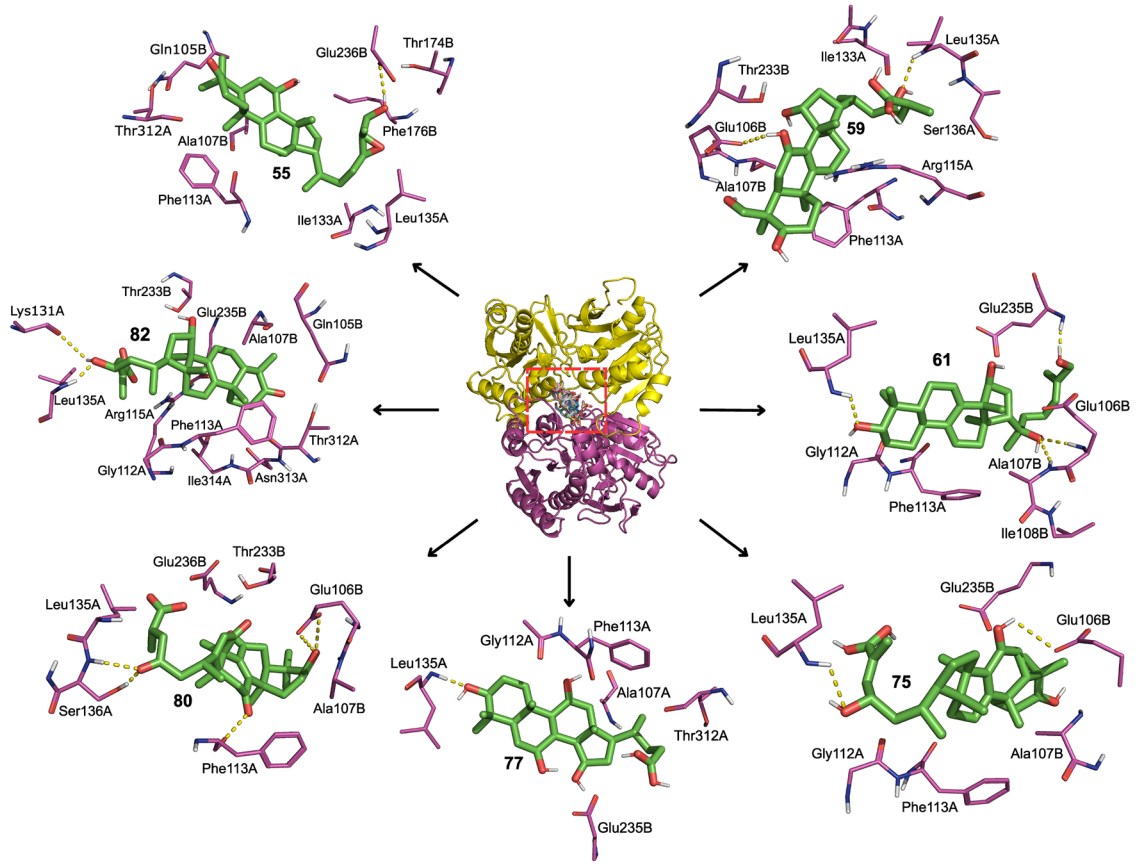

Figure 6. Hydrogen bond interactions involved in receptor-ligand molecular coupling. Ligands are shown in green, and amino acid residues of targets are shown in magenta. The yellow dotted lines are hydrogen bond interactions.

Glu236B); ligand **59** has two hydrogen bond interactions (residues Glu106B and Leu135A); ligand **61** has four hydrogen bond interactions (residues Glu106B, Ala107B, Leu135A and Glu235B); ligand **75** has two hydrogen bond interactions (residues Glu106B and Leu135B); ligand **77** has one hydrogen bond interaction (residue Leu135A); ligand **80** has five hydrogen bond interactions (two interactions with the acidic portion of the Ala107B residue, followed by two hydrogen bond interactions with the Ser136A residue, and one hydrogen bond interaction with the Phe113A residue); ligand **82** has two hydrogen bond interactions (residues Lys131A and Leu135A).

Induced fitting

Compounds **55**, **59**, **61**, **75**, **77**, **80**, and **82** were used as ligands to study the receptor-ligand stability of the complex through MD simulations. The study used the clusters that presented better results from the ensemble docking. MD simulations lasting 400 ns were run for each complex, and the resulting trajectories were subjected to RMSD analysis for both the protein and ligand.

It was observed that only ligands **55**, **75**, **80**, and **82** demonstrated stabilities along the proposed trajectory. As ligands **59**, **61**, and **77** did not show stability during the long 400 ns simulation, they were excluded from the subsequent analysis. Therefore, in addition to the RMSD, the protein root-mean-square fluctuation (RMSF), the ligand root-mean-square fluctuation, and the hydrogen bonding interactions associated with ligands **55**, **75**, **80**, and **82** were evaluated. This refined analysis process provided a more in-depth understanding of the stability and dynamic behavior of the NMDA receptor complexes, GluN1-GluN2B subunits and ligands in question.

To assess the structural stability of the four stable complexes, RMSD of the protein and the ligand were analyzed over the 400 ns simulation (Figure 7). A comparison of the panels in Figure 7 reveals that all systems reached equilibrium, but with distinct kinetics. The complex with ligand **75** (Figure 7b) was the quickest to reach equilibrium, doing so at approximately 60 ns and maintaining an average protein backbone RMSD of about 0.4 nm. On the other hand, the complex with ligand **82** (Figure 7d), while taking slightly longer to fully settle (stabilizing after 130 ns), did so in a notably more stable state, with a lower average RMSD of about 0.3 nm. This suggests that ligand **82** induces a more compact and rigid final conformation in the receptor. The complexes with ligands **55** (Figure 7a) and **80** (Figure 7c) required longer simulation times to equilibrate, reaching stable plateaus after approximately 220 and 190 ns, respectively.

The analysis of the ligand's own RMSD (red lines in Figure 7) indicates its positional stability within the binding site. Ligand **82** demonstrated exceptional

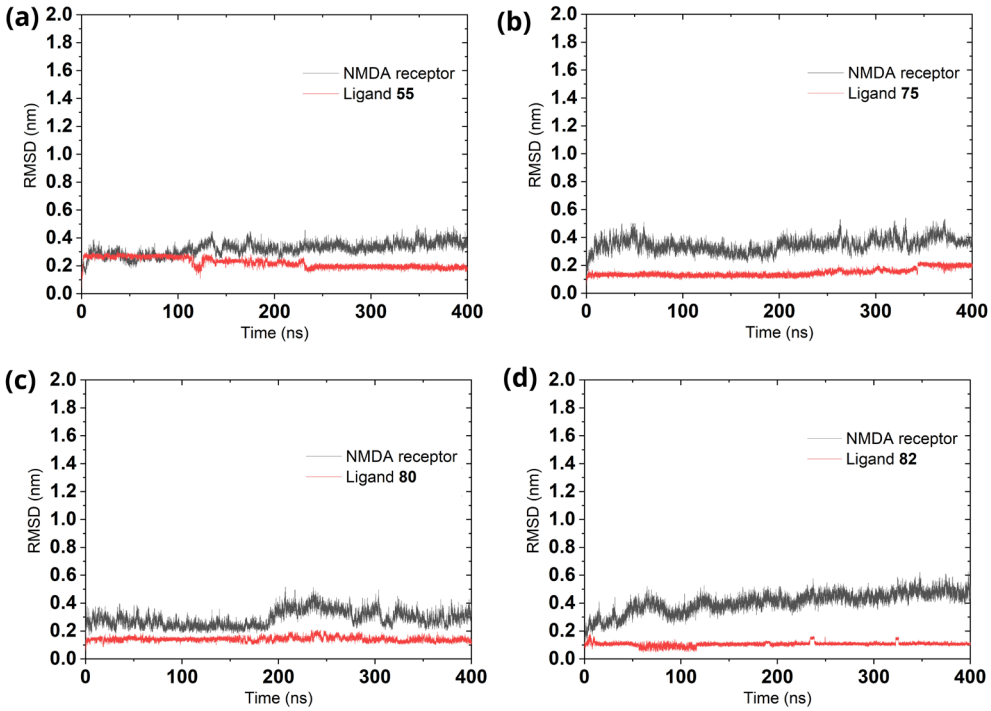

Figure 7. Structural stability of the NMDA receptor-ligand complexes. Root-mean-square deviation (RMSD) over 400 ns for complexes with ligands (a) **55**, (b) **75**, (c) **80**, and (d) **82**. The black line is the protein backbone (Cα) RMSD, showing overall complex stability. The red line is the ligand heavy-atom RMSD, showing its positional stability.

positional stability, with minimal fluctuations throughout the simulation. Ligand **75** also proved to be highly stable. In contrast, ligands **55** and **80** exhibited greater mobility within the binding site, suggesting that while they form stable complexes, their binding poses are more dynamic.

To investigate how each ligand affects the flexibility of the receptor, the RMSF *per* residue was calculated for each complex (Figure 8). In all four systems, a common pattern is observed: the highest fluctuations occur in the linker region connecting the two lobes of the binding domain (residues ca. 110-240), which is consistent with this region's known role in accommodating the ligand.

However, a comparison between the panels in Figure 8 reveals differences in the magnitude of these fluctuations. The complex with ligand **80** (Figure 8c) induced the most pronounced flexibility in this region, with RMSF values reaching up to 0.6 nm. In contrast, the complexes with ligands **75** (Figure 8b) and **82** (Figure 8d) displayed lower RMSF values (max 0.45 nm), which correlates with their more stable binding modes observed in the RMSD analysis. The complex with ligand **55** (Figure 8a) showed an intermediate fluctuation profile.

The intrinsic flexibility of each ligand within the binding site was comparatively evaluated via the RMSF of its heavy atoms (Figure 9). The atom numbering corresponds to the 2D structures presented in the SI section (Figure S4). The overlaid plot allows for a direct comparison, revealing that ligand **82** (orange line) is the most rigid, with consistently low fluctuations (below 0.15 nm), which corroborates its high positional stability. Ligand **55** (purple line) is the most flexible, exhibiting significant fluctuation peaks, especially for the atoms of the epoxy moiety and the terminal hydroxyl group (atoms 33 and 34). Ligands **75** (blue line) and **80** (yellow line) show intermediate mobility, concentrated mainly in their side chains containing the carboxylic acid group (e.g., atoms 33 and 34 for ligand **75**; atoms 34 and 36 for ligand **80**). These differences in ligand flexibility provide a structural basis for understanding the variations in stability and binding affinity observed among the four lead candidates.

To further rationalize the observed stabilities, the hydrogen bonding interactions between each ligand and the receptor were monitored throughout the simulations. A detailed analysis of the number of hydrogen bonds formed over time for each complex is provided in the SI section (Figure S5). This analysis reveals a clear correlation between the extent of hydrogen bonding and the stability of the complex. Notably, ligand **82**, the most stable candidate, maintained the highest average number of hydrogen bonds (approximately 5), providing a strong energetic basis for its low RMSD and RMSF values. Ligand **75** also formed a robust network of interactions. In contrast, ligands **55** and **80** displayed a sparser hydrogen bond network, which is consistent with their greater flexibility. These findings underscore the critical role of specific hydrogen bonding in anchoring the ligands within the binding pocket and stabilizing the overall protein-ligand complex.

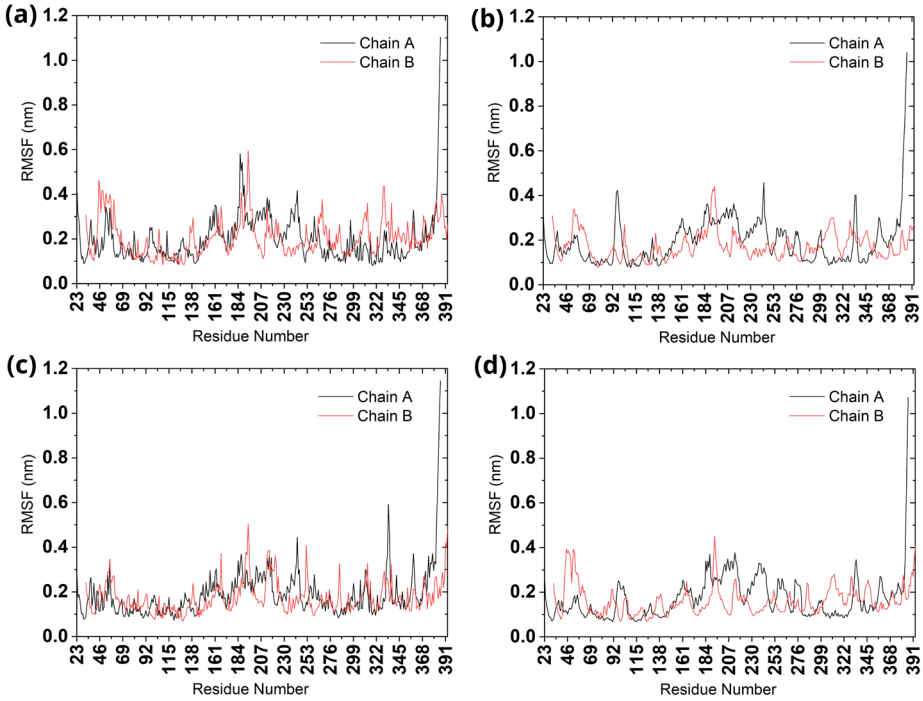

Figure 8. Flexibility of the NMDA receptor upon ligand binding. Root-mean-square fluctuation (RMSF) of protein Cα atoms for complexes with (a) **55**, (b) **75**, (c) **80**, and (d) **82**. Black and red lines represent chains A and B, respectively.

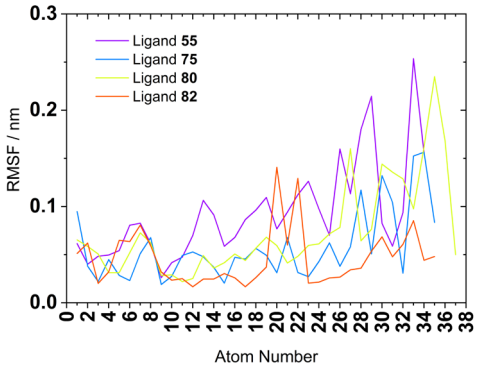

Figure 9. Comparative internal flexibility of the bound ligands. Overlaid root-mean-square fluctuation (RMSF) of heavy atoms for ligands **55** (purple), **75** (blue), **80** (yellow), and **82** (orange).

Binding energy calculation

To evaluate the affinity of the NMDA receptor, GluN1-GluN2B subunits, with ligands **55**, **75**, **80**, and **82**, a study was carried out using the MM-GBSA technique, using the gmx_MMPBSA tool.[53] This technique has been widely used to calculate the interaction energy between receptor-ligand, considering that it requires a set of snapshots from molecular dynamics simulations, thus using relatively stable trajectories.[69] For this work, 100 frames were used from the last 10 ns of each molecular dynamics' simulation (390 to 400 ns). To determine the optimal dielectric parameters for the MM-GBSA calculations, we first evaluated the effect of the external solvent dielectric constant (ε_{sol}). With a fixed internal protein dielectric (ε_{pro} = 2), we performed comparative calculations using ε_{sol} values of 20, 40, and 80. The results, detailed in Table S4 (SI section), demonstrated that ε_{sol} = 20 consistently yielded the most favorable (i.e., most negative) binding energy values across our lead compounds. Based on this direct comparison, the dielectric constants for the protein and solvent were set to 2 and 20, respectively, for all subsequent analyses.

A study of fluctuations in the total interaction energy was also carried out, carefully analyzing the energetic contribution of each residue within 10.0 Å of ligands **55**, **75**, **80**, and **82**. Analyzing Figure 10, small changes in the contribution of each residue, confirmed by variations evidenced in the total binding energy calculated under different values of the dielectric constant of the solvent (20, 40, or 80), it was observed in all complexes that the oscillations in binding energy along the radial distance remained consistent, suggesting invariability in the contribution of residues regardless of the dielectric parameters used.

Analyzing the decomposition energy of MM-GBSA up to 10.0 Å from ligand 55 with NMDA receptor, GluN1-GluN2B subunits, the interaction was around –22.32 kcal mol^{-1}, the interaction energy of the residues located within 5.0 Å presented a value of –11.63 kcal mol^{-1}, representing approximately 52.11% of this total interaction. The interaction energy within 6.0 Å represents around 86.69% of the total energy, with a value of –19.35 kcal mol^{-1}. For the complex formed between ligand **75** and the NMDA receptor, GluN1-GluN2B subunits, the calculated total energy was –32.16 kcal mol^{-1}, while residues within 6.0 Å represent about 89.92% of this interaction, with a value of –28.92 kcal mol^{-1}. For the complex formed between the GluN1-Glun2B subunits of the NMDA receptor and ligand **80**, the calculated total energy was –20.20 kcal mol^{-1}, while the residues within 6.0 Å represent approximately 98.22% of this interaction, with a value of –19.84 kcal mol^{-1}. For the complex formed between the GluN1-GluN2B subunits of the NMDA receptor and ligand **82**, the calculated total energy was –34.25 kcal mol^{-1}, while the residues within 6.0 Å represent approximately 82.83% of this interaction, with a value of –28.37 kcal mol^{-1}. The interaction energy after 9.0 Å did not show significant oscillations and no amino acid residues with a radius of 2.0 Å were detected. For clarity, the calculated individual energy degradation values of the NMDA receptor residues, GluN1-GluN2B subunits, are shown in Tables S3-S6 (SI section).

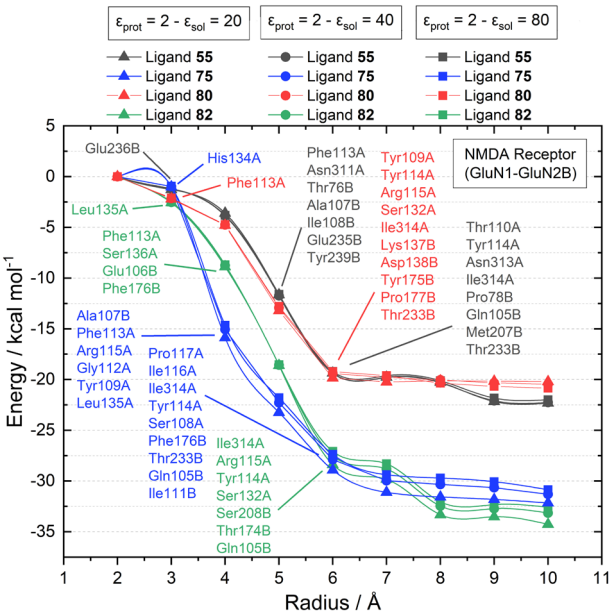

Figure 10. Variations in the individual contribution energy of residues to the total interaction energy for the NMDA receptor complexes, GluN1-GluN2B subunits and ligands **55**, **75**, **80**, and **82** at different values of the solvent dielectric constant. Interaction energy in kcal mol^{-1} and distance in angstroms (Å).

The values of van der Waals interactions (ΔE_{vdw}), shown in Table S2 (SI section), are important in complex stabilization and molecular recognition, especially when

molecules are close together.[70] For ligands **55**, **75**, **80**, and **82**, these interactions played a crucial role in affinity with the NMDA receptor, GluN1-GluN2B subunits, compared to electrostatic forces (ΔE_{elec}), with the main contribution to formation of the receptor-ligand complex being attributed to van der Waals interactions. The values for each receptor-ligand complex were −50.67 kcal mol^{-1} for ligand **55**, −54.64 kcal mol^{-1} for ligand **75**, −49.00 kcal mol^{-1} for ligand **80**, and −55.70 kcal mol^{-1} for ligand **82**.

As for electrostatic energy (ΔE_{elec}), the values were −14.19, 78.38, 163.30 and 78.83 kcal mol^{-1}, for ligands **55**, **75**, **80**, and **82**, respectively. As for the solvation energy (ΔG_{SOLV}), the values were 14.78, −83.58, −154.70 and −82.64 kcal mol^{-1}, respectively. Significant differences in electrostatic energy and solvation energy are noted between ligand **55** and ligands **75**, **80**, and **82**, in which the electrostatic contribution to complex formation was unfavorable for ligands **75**, **80**, and **82**, but was compensated by solvation energy, therefore being the main energy of formation of these complexes. This perceived compensation can influence the overall binding affinity ($\Delta G_{binding}$) of ligands with their receptor. In this context, it is important to consider individual solvation contributions when investigating binding affinity. Furthermore, the subdivision of this energy into polar (ΔE_{GB}) and non-polar solvation terms (ΔE_{SURF}), is essential for understanding the interactions between solvent and solute atoms.[71,72] However, the electrostatic energy value for the NMDA receptor complex, GluN1-GluN2B subunits and ligand **80** presented a very high value, being extremely unfavorable for the formation of the complex.

Analyzing the binding affinity ($\Delta G_{binding}$) of each complex and comparing it with the interaction energy from the ensemble docking simulations, we can see that ligand **55** presented values of −50.08 and −11.238 kcal mol^{-1}, respectively, as shown in Table 4. Ligands **75**, **80**, and **82** showed binding affinity of −59.84, −40.40, and −59.52 kcal mol^{-1}, respectively, while the interactions energy of the docking ensemble were very similar, −10.982, −10.948, and −10.915 kcal mol^{-1}, respectively.

Table 4. Results of the interaction energy calculations obtained during ensemble docking and through the MM-GBSA method for each receptor-substrate complex **55**, **75**, **80**, and **82**

Ligand	MM-GBSA ± sd / (kcal mol^{-1})	Ensemble docking / (kcal mol^{-1})
55	−50.08 ± 2.6	−11.238
75	−59.84 ± 2.0	−10.982
80	−40.40 ± 2.6	−10.948
82	−59.52 ± 3.0	−10.915

MM-GBSA: Molecular Mechanics Generalized-Born Surface Area; sd: standard deviation.

Individual contributions of residues

To identify essential residues that contribute to the receptor-ligand interaction and understand the role of individual residues in the binding mechanism with ligands **55**, **75**, **80**, and **82**, the energy decomposition was evaluated using the MM-GBSA technique. In this case, the dielectric constant of the protein (ε_{pro}) and solvent (ε_{sol}) were set at 2 and 20, respectively (horizontal bars in Figure 11). During this investigation, more favorable contributions were identified, and the complexes exhibited distinct energetic decompositions for the binding free energy. In the complex formed by the NMDA receptor, GluN1-GluN2B subunits and ligand **55**, the main contributions were from the following residues: Phe113A (−2.52 kcal mol^{-1}), Arg115A (−1.39 kcal mol^{-1}), Thr312A (−1.88 kcal mol^{-1}), Ile314A (−1.72 kcal mol^{-1}), Gln105B (−1.72 kcal mo^{-1}) and Glu235B (−1.79 kcal mol^{-1}), as shown in Figure 11 in green bars. In the complex formed by the NMDA receptor, GluN1-GluN2B subunits and ligand **75**, the main contributions were from the following residues: Gly112A (−1.69 kcal mol^{-1}), Phe113A (−2.39 kcal mol^{-1}), Arg115A (−6.91 kcal mol^{-1}), Ile133A (−1.45 kcal mol^{-1}), Leu135A (−1.53 kcal mol^{-1}), Ser136A (−2.06 kcal mol^{-1}), and Pro177B (−1.73 kcal mol^{-1}), as shown in Figure 11 in purple bars. For the complex formed by the NMDA receptor, GluN1-GluN2B subunits and ligand **80**, the main contributions were from the following residues: Tyr109A (−1.78 kcal mol^{-1}), Phe113A (−2.19 kcal mol^{-1}), Ile133A (−1.60 kcal mol^{-1}), Leu135A (−1.98 kcal mol^{-1}), Gln110B (−3.05 kcal mol^{-1}), and Phe176B (−1.46 kcal mol^{-1}), the Asp113B residue presented a repulsion energy of 1.04 kcal mol^{-1}, as shown in Figure 11 in yellow bars. For the complex formed by the NMDA receptor, GluN1-GluN2B subunits and ligand **82**, the main contributions were from the following residues: Tyr109A (−1.36 kcal mol^{-1}), Phe113A (−1.91 kcal mol^{-1}), Arg115A (−7.36 kcal mol^{-1}), Leu135A (−2.57 kcal mol^{-1}), Leu136A (−1.35 kcal mol^{-1}), and Phe176B (−2.14 kcal mol^{-1}), as shown in Figure 11 in orange bars.

An analysis of the hydrophobic contacts and hydrogen bond interactions between the residues of the NMDA receptor, GluN1-GluN2B subunits, with ligands **55**, **75**, **80**, and **82** was also carried out. For receptor-ligand complexes, the interaction was stabilized by a combination of hydrophobic contacts and hydrogen bonding interactions (Figure 12). For the NMDA receptor complex, GluN1-GluN2B subunits, and ligand **55**, hydrophobic contacts were observed mainly between residues Phe113A (ΔE = −2.52 kcal mol^{-1}), Thr312A (ΔE = −1.88 kcal mol^{-1}), Thr76B (ΔE = −1.08 kcal mol^{-1}), Pro78B

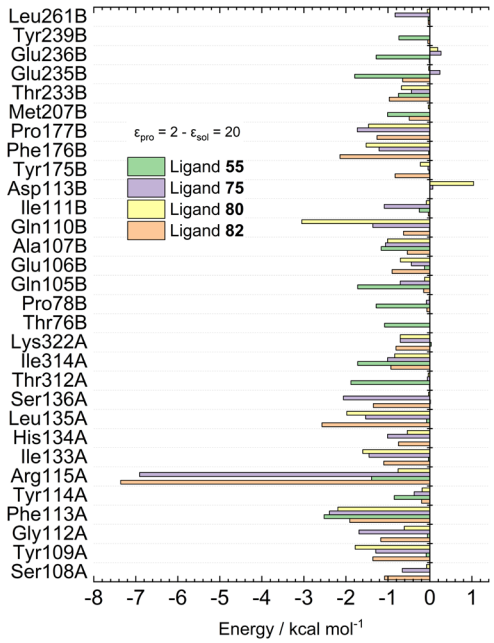

Figure 11. *Per*-residue decomposition of the interaction energy between the GluN1-GluN2B subunits of the NMDA receptor and the ligands, calculated by MM-GBSA. Only residues within 10 Å of each ligand were considered. Bars represent the residues with the highest contributions to the binding energies of ligands **55** (green), **75** (purple), **80** (yellow), and **82** (orange).

($\Delta E = -1.28$ kcal mol^{-1}) and Met207B ($\Delta E = -1.01$ kcal mol^{-1}). Furthermore, hydrogen bond interactions were identified with residues Arg115A ($\Delta E = -1.39$ kcal mol^{-1}), Figure 12a.

As for the NMDA receptor complex, GluN1-GluN2B subunits and ligand **75** (Figure 12b), hydrophobic contacts were observed mainly between residues Gly112A ($\Delta E = -1.69$ kcal mol^{-1}), Phe113A ($\Delta E = -2.39$ kcal mol^{-1}), His134A ($\Delta E = -1.01$ kcal mol^{-1}) and Ala107B ($\Delta E = -1.06$ kcal mol^{-1}). Furthermore, significant hydrogen bond interactions were identified with residues Arg115A ($\Delta E = -6.91$ kcal mol^{-1}), Ile133A ($\Delta E = -1.45$ kcal mol^{-1}), Leu135A ($\Delta E = -1.53$ kcal mol^{-1}) and Ser136A ($\Delta E = -2.06$ kcal mol^{-1}). Analyzing Figure 12c, which shows the interaction formed by the NMDA receptor complex, GluN1-GluN2B subunits and ligand **80**, hydrophobic contacts were observed mainly between Tyr109A residues ($\Delta E = -1.78$ kcal mol^{-1}), Phe113A ($\Delta E = -2.19$ kcal mol^{-1}), Leu135A ($\Delta E = -1.98$ kcal mol^{-1}), Phe176B ($\Delta E = -1.52$ kcal mol^{-1}) and Pro177B ($\Delta E = -1.46$ kcal mol^{-1}). Furthermore, a significant hydrogen bond interaction was identified with the Glu106B residue ($\Delta E = -0.71$ kcal mol^{-1}) and Gln110B ($\Delta E = -3.05$ kcal mol^{-1}). Analyzing Figure 12d, which shows the interaction formed by the NMDA receptor complex, GluN1-GluN2B subunits and ligand **82**, hydrophobic contacts were observed mainly between Phe113A residues ($\Delta E = -1.91$ kcal mol^{-1}), Leu135A ($\Delta E = -2.57$ kcal mol^{-1}) and Ser136A ($\Delta E = -1.35$ kcal mol^{-1}). Furthermore, a significant hydrogen bond interaction was identified with the Arg115A residue ($\Delta E = -7.36$ kcal mol^{-1}).

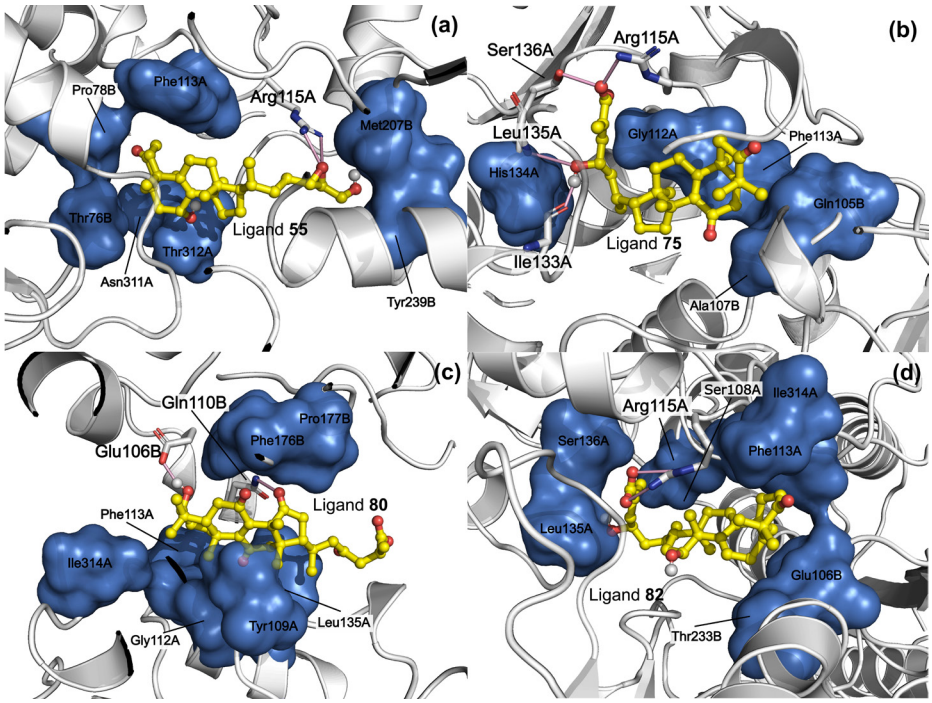

Figure 12. Spatial organization of the main residues involved in hydrophobic contacts and hydrogen bond interactions between the GluN1-GluN2B subunits and (a) ligand **55**, (b) ligand **75**, (c) ligand **80**, and (d) ligand **82**. Protein structure is depicted as white cartoon representation. Ligands **55**, **75**, **80**, and **82** are shown as yellow sticks. Hydrophobic contacts are highlighted as a blue surface, while residues involved in hydrogen bonds are represented by white sticks and hydrogen bonds are indicated by pink dashes.

Structure-activity relationship of the NMDA receptor ligands

For the structure-activity relationship (SAR) study, the compounds were classified according to their carbon skeleton into two groups. Table 5 displays the compounds that feature an 8(9)-ene carbon skeleton, while Table 6 presents the compounds with a 7(8),9(11)-diene skeleton. These structures generally differ in the position and number of unsaturations present in the main skeleton. Regarding the lateral carbon chain, these triterpenes feature oxygenated organic functions such as alcohol, carboxylic acid, ketone, and epoxy ether.

To better understand the impact of functional groups on ligand affinity, we examined how specific substituents at different positions of the lanostane skeleton influenced the molecular docking results, dynamic stability, and MM-GBSA binding energies. Overall, the presence of oxygenated groups (alcohol, carboxylic acid, ketone, and epoxy ether) at the side chain (C-17 position) appeared to be a key factor for binding affinity and stability.

For instance, ligand **82**, which displayed the best MM-GBSA binding energy (–59.52 kcal mol^{-1}), features a ketone at R_1, a hydroxyl at R_3, and a side chain with both hydroxyl and carboxylic acid groups. This configuration likely enhances hydrogen bond formation and contributes to high stability, as evidenced by its low RMSD and high number of persistent hydrogen bonds during the MD simulation. In contrast, ligand **55**, which also contains an epoxide and hydroxyl on the side chain, showed a slightly less favorable energy (–50.08 kcal mol^{-1}) and greater internal flexibility, suggesting that while polar groups favor interaction, the rigidity imposed by epoxide rings may reduce conformational adaptability.

Comparison of the chemical structures of ligands **75** and **80** highlights how subtle changes in the chemical structure modulate activity. Ligand **75**, with two carbonyl groups at R_1 and R_3 and a hydroxyl-carboxyl side chain, presented a strong binding energy (–59.84 kcal mol^{-1}). In contrast, ligand **80**, though featuring multiple carbonyl

Table 5. Structural features and binding parameters of lanostane-type triterpenes with an 8(9)-ene skeleton, including the main substituents (R_1-R_5), side chain functionality at C-17, ensemble docking score, molecular dynamics (MD) stability over 400 ns, and binding free energy values obtained by MM-GBSA calculations

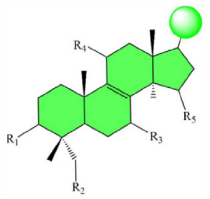

Compound	R_1, R_2, R_3, R_4, R_5	C-17 side chain moiety	Ensemble docking / (kcal mol^{-1})	MD stability (400 ns)	MM-GBSA[a] / (kcal mol^{-1})
55	=O, –H, –OH, –H, –H	epox, –OH	–11.238	stable	–50.08 ± 2.6
59	=O, –OH, =O, –H, –OH	=O, –COOH	–11.192	unstable	N/A
75	=O, –H, =O, –H, –H	–OH, –COOH	–10.982	stable	–59.84 ± 2.0
77	–OH, –H, –OH, =O, =O	–OH, –COOH	–10.966	unstable	N/A
80	–OH, –H, =O, =O, =O	=O, –COOH	–10.948	stable	–40.40 ± 2.6

[a]N/A: not applicable, as MM-GBSA calculations were not performed on unstable complexes.

Table 6. Structural features and binding parameters of lanostane-type triterpenes with a 7(8),9(11)-diene skeleton, summarizing the substituents (R_1-R_3), side chain groups at C-17, ensemble docking results, MD stability assessment (400 ns), and binding free energy values obtained by MM-GBSA calculations

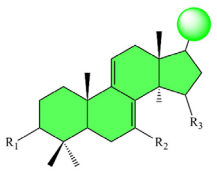

Compound	R_1, R_2, R_3	C-17 side chain moiety	Ensemble docking / (kcal mol^{-1})	MD stability (400 ns)	MM-GBSA[a] / (kcal mol^{-1})
61	–OH, –H, –OH	–OH, –OH	–11.189	unstable	N/A
82	=O, –H, –OH	–OH, –COOH	–10.915	stable	–59.52 ± 3.0

[a]N/A: not applicable, as MM-GBSA calculations were not performed on unstable complexes.

groups including an unprecedented double bond system, had lower binding energy (–40.40 kcal mol^{-1}), possibly due to its less favorable electrostatic profile and increased ligand mobility within the binding site.

These findings indicate that a balanced distribution of hydrogen bond donors/acceptors, combined with moderate molecular flexibility, contributes positively to receptor binding. Furthermore, the carbonyl and hydroxyl functionalities at R_1-R_5, especially when paired with a carboxylic acid at the C-17 side chain, enhance both docking affinity and complex stability.

Conclusions

In this study, we have employed a robust pipeline of molecular simulation to identify, among 821 lanostane-type triterpenes, seven compounds with ability to bind to the GluN1-GluN2B subunit of NMDA receptor. Pharmacokinetic simulations revealed that compounds **55**, **59**, **61**, **75**, **77**, **80**, and **82** demonstrate promising central nervous system penetration with a low potential for adverse effects. Additionally, these compounds exhibit lipophilicity, hepatotoxicity, and mutagenicity profiles comparable to those of ifenprodil, suggesting that they possess favorable characteristics for drug development. Furthermore, molecular dynamics simulations and MM-GBSA calculations characterized the binding profile of each molecule, identifying compounds **55**, **75**, and **82** as the most promising candidates for NMDAR inhibition. This study highlights the potential of lanostane-type triterpenes as therapeutic candidates for neuropsychiatric disorders associated with NMDAR dysfunction, representing a significant advancement in the development of selective and effective NMDAR modulators.

Supplementary Information

Supplementary information is available free of charge at http://jbcs.sbq.org.br as a PDF file.

Data Availability Statement

All data generated and/or analyzed during this study are included in this published article and its supplementary information files.

Acknowledgments

We are grateful to the Coordenação de Aperfeiçoamento de Ensino Superior (CAPES) for the financial support (Finance Code 001-PROEX 23038.000509/2020-82. AUXPE No. 1227/2020). Jonatas M. Negreiro thanks Fundação Cearense de Apoio ao Desenvolvimento Científico e Tecnológico (FUNCAP) (process: BMD-0008-01997.01.20/22) and Conselho Nacional de Desenvolvimento Científico e Tecnológico (CNPq) (process: 141007/2025-7) for his doctorate sponsorships. José A. C. Oliveira (Doctorate sponsorship; process: 160441/2021-8), Maria C. F. de Oliveira (research grant; processes: 305148/2023-0; 441326/2023-4), Marcos C. de Mattos (research grant; processes: 306289/2021-0; 402631/2023-4), Danielle S. Macedo (research grant; process: 309011/2022-1) and Geancarlo Zanatta (grant: 408135/2023-9) thank Conselho Nacional de Desenvolvimento Científico e Tecnológico (CNPq). We are also thankful to the Centro Nacional de Supercomputação at the Federal University of Rio Grande do Sul (CESUP/UFRGS) for the computer cluster facilities and SDumont cluster in the National Laboratory for Scientific Computing (LNCC/MCTI, Brazil).

Author Contributions

Jonatas M. Negreiro, José A. C. Oliveira was responsible for for investigation, data curation; Fátima M. Nunes, Francisco G. Barbosa, Jair Mafezoli, Marcos C. Mattos, Danielle S. Macedo for supervision, data curation, writing original draft; Geancarlo Zanatta, Maria C. F. Oliveira for conceptualization, project administration, funding acquisition, writing review and editing.

References

1. Paoletti, P.; *Eur. J. Neurosci.* **2011**, *33*, 1351. [Crossref]
2. Newcomer, J. W.; Farber, N. B.; Olney, J. W.; *Dialogues Clin. Neurosci.* **2000**, *2*, 219. [Crossref]
3. Chen, S.; Xu, D.; Fan, L.; Fang, Z.; Wang, X.; Li, M.; *Front. Mol. Neurosci.* **2022**, *14*, 797253. [Crossref]
4. Li, Q.-Q.; Lin, X.; Shi, Y. S.; *Adv. Neurol.* **2022**, *1*, 148. [Crossref]
5. Nikolin, S.; Rodgers, A.; Schwaab, A.; Bahji, A.; Zarate, C.; Vazquez, G.; Loo, C.; *eClinicalMedicine* **2023**, *62*, 102127. [Crossref]
6. Sinyor, M.; Schaffer, A.; Levitt, A.; *Can. Psychiatr. Assoc. J.* **2010**, *55*, 126. [Crossref]
7. Tang, B. C.; Wang, Y. T.; Ren, J.; *Ibrain* **2023**, *9*, 340. [Crossref]
8. Sandström, K. O.; Baltzersen, O. B.; Marsman, A.; Lemvigh, C. K.; Boer, V. O.; Bojesen, K. B.; Nielsen, M.; Lundell, H.; Sulaiman, D. K.; Sørensen, M. E.; Fagerlund, B.; Lahti, A. C.; Syeda, W. T.; Pantelis, C.; Petersen, E. T.; Glenthøj, B. Y.; Siebner, H. R.; Ebdrup, B. H.; *Front. Mol. Psychiatry* **2022**, *13*, 889572. [Crossref]
9. Zhou, H. Y.; Chen, S. R.; Pan, H. L.; *Expert Rev. Clin. Pharmacol.* **2011**, *4*, 379. [Crossref]
10. Petrenko, A. B.; Yamakura, T.; Sakimura, K.; Baba, H.; *Eur. J. Pharmacol.* **2014**, *723*, 29. [Crossref]
11. Short, B.; Fong, J.; Galvez, V.; Shelker, W.; Loo, C. K.; *Lancet Psychiatry* **2018**, *5*, 65. [Crossref]

12. Hanson, J. E.; Weber, M.; Meilandt, W. J.; Wu, T.; Luu, T.; Deng, L.; Shamloo, M.; Sheng, M.; Scearce-Levie, K.; Zhou, Q.; *Neuropsychopharmacology* **2013**, *38*, 1221. [Crossref]
13. Gu, Q.; Wang, C. In *Handbook of Developmental Neurotoxicology*, 2nd ed.; Slikker Jr., W.; Paule, M. G.; Wang, C., eds.; Academic Press: London, UK, 2018, ch. 18. [Crossref]
14. Camargo, A.; Dalmagro, A. P.; Rebelo, A. M.; Reinke, C. K.; Zeni, A. L. B.; *Nat. Prod. Res.* **2022**, *36*, 4692. [Crossref]
15. Tantipongpiradet, A.; Monthakantirat, O.; Vipatpakpaiboon, O.; Khampukdee, C.; Umehara, K.; Noguchi, H.; Fujiwara, H.; Matsumoto, K.; Sekeroglu, N.; Kijjoa, A.; Chulikhit, Y.; *Molecules* **2019**, *24*, 4569. [Crossref]
16. Wang, G.; Lei, C.; Tian, Y.; Wang, Y.; Zhang, L.; Zhang, R.; *Front. Pharmacol.* **2019**, *10*, 1034. [Crossref]
17. Khan, I.; Karim, N.; Ahmad, W.; Abdelhalim, A.; Chebib, M.; *J. Evidence-Based Complementary Altern. Med.* **2016**, *2016*, 1215393. [Crossref]
18. Xian, Y.-F.; Fan, D.; Ip, S.-P.; Mao, Q.-Q.; Lin, Z.-X.; *Neurochem. Res.* **2017**, *42*, 678. [Crossref]
19. Liang, M.; Du, Y.; Li, W.; Yin, X.; Yang, N.; Qie, A.; Lebaron, T. W.; Zhang, J.; Chen, H.; Shi, H.; *Biol. Pharm. Bull.* **2018**, *41*, 1040. [Crossref]
20. Chen, L.; Li, M.; Yang, Z.; Tao, W.; Wang, P.; Tian, X.; Li, X.; Wang, W.; *J. Ethnopharmacol.* **2020**, *257*, 112829. [Crossref]
21. Boncan, D. A. T.; Tsang, S. S. K.; Li, C.; Lee, I. H. T.; Lam, H.-M.; Chan, T.-F.; Hui, J. H. L.; *Int. J. Mol. Sci.* **2020**, *21*, 7382. [Crossref]
22. Yurchenko, E. A.; Kolesnikova, S. A.; Lyakhova, E. G.; Menchinskaya, E. S.; Pislyagin, E. A.; Chingizova, E. A.; Aminin, D. L.; *Molecules* **2020**, *25*, 5397. [Crossref]
23. Xia, Q.; Zhang, H.; Sun, X.; Zhao, H.; Wu, L.; Zhu, D.; Yang, G.; Shao, Y.; Zhang, X.; Mao, X.; Zhang, L.; She, G.; *Molecules* **2014**, *19*, 17478. [Crossref]
24. Ruszkowski, P.; Bobkiewicz-Kozlowska, T.; *Mini-Rev. Org. Chem.* **2014**, *11*, 307. [Crossref]
25. Gasiorowska, A.; Wydrych, M.; Drapich, P.; Zadrozny, M.; Steczkowska, M.; Niewiadomski, W.; Niewiadomska, G.; *Front. Aging Neurosci.* **2021**, *13*, 654931. [Crossref]
26. Guo, Y. F.; Feng, Y. Z.; Xu, J. Y.; Dong, M. Y.; Yang, A. A.; Gao, J. M.; Yin, X.; *Bioorg. Chem.* **2025**, *163*, 108757. [Crossref]
27. Oliveira, J. A. C.; Negreiro, J. M.; Nunes, F. M.; Barbosa, F. G.; Mafezoli, J.; Mattos, M. C.; Fernandes, M. C. R.; Pessoa, C.; Furtado, C. L. M.; Zanatta, G.; Oliveira, M. C. F.; *ACS Omega* **2024**, *9*, 50844. [Crossref]
28. Stroebel, D.; Buhl, D. L.; Knafels, J. D.; Chanda, P. K.; Green, M.; Sciabola, S.; Mony, L.; Paoletti, P.; Pandit, J.; *Mol. Pharmacol.* **2016**, *89*, 541. [Crossref]
29. Biasini, M.; Bienert, S.; Waterhouse, A.; Arnold, K.; Studer, G.; Schmidt, T.; Kiefer, F.; Cassarino, T. G.; Bertoni, M.; Bordoli, L.; Schwede, T.; *Nucleic Acids Res.* **2014**, *42*, 252. [Crossref]
30. Waterhouse, A.; Bertoni, M.; Bienert, S.; Studer, G.; Tauriello, G.; Gumienny, R.; Heer, F. T.; de Beer, T. A. P.; Rempfer, C.; Bordoli, L.; Lepore, R.; Schwede, T.; *Nucleic Acids Res.* **2018**, *46*, W296. [Crossref]
31. *SWISS-MODEL*; SIB Swiss Institute of Bioinformatics; University of Basel, Switzerland, 2003.
32. Apweiler, R.; Bairoch, A.; Wu, C. H.; Winona, C.; Barker, W. C.; Boeckmann, B.; Ferro, S.; Gasteiger, E.; Huang, H.; Lopez, R.; Magrane, M.; Martin, M. J.; Natale, D. A.; O'Donovan, C.; Redaschi, N.; Yeh, L.-S. L.; *Nucleic Acids Res.* **2004**, *32*, D115. [Crossref]
33. Bateman, A.; Martin, M. J.; O'Donovan, C.; Magrane, M.; Alpi, E.; Antunes, R.; Bely, B.; Bingley, M.; Bonilla, C.; Britto, R.; Bursteinas, B.; Bye-AJee, H.; Cowley, A.; Da Silva, A.; De Giorgi, M.; Dogan, T.; Fazzini, F.; Castro, L. G.; Figueira, L.; Garmiri, P.; Georghiou, G.; Gonzalez, D.; Hatton-Ellis, E.; Li, W.; Liu, W.; Lopez, R.; Luo, J.; Lussi, Y.; MacDougall, A.; Nightingale, A.; Palka, B.; Pichler, K.; Poggioli, D.; Pundir, S.; Pureza, L.; Qi, G.; Rosanoff, S.; Saidi, R.; Sawford, T.; Shypitsyna, A.; Speretta, E.; Turner, E.; Tyagi, N.; Volynkin, V.; Wardell, T.; Warner, K.; Watkins, X.; Zaru, R.; Zellner, H.; Xenarios, I.; Bougueleret, L.; Bridge, A.; Poux, S.; Redaschi, N.; Aimo, L.; ArgoudPuy, G.; Auchincloss, A.; Axelsen, K.; Bansal, P.; Baratin, D.; Blatter, M. C.; Boeckmann, B.; Bolleman, J.; Boutet, E.; Breuza, L.; Casal-Casas, C.; de Castro, E.; Coudert, E.; Cuche, B.; Doche, M.; Dornevil, D.; Duvaud, S.; Estreicher, A.; Famiglietti, L.; Feuermann, M.; Gasteiger, E.; Gehant, S.; Gerritsen, V.; Gos, A.; Gruaz-Gumowski, N.; Hinz, U.; Hulo, C.; Jungo, F.; Keller, G.; Lara, V.; Lemercier, P.; Lieberherr, D.; Lombardot, T.; Martin, X.; Masson, P.; Morgat, A.; Neto, T.; Nouspikel, N.; Paesano, S.; Pedruzzi, I.; Pilbout, S.; Pozzato, M.; Pruess, M.; Rivoire, C.; Roechert, B.; Schneider, M.; Sigrist, C.; Sonesson, K.; Staehli, S.; Stutz, A.; Sundaram, S.; Tognolli, M.; Verbregue, L.; Veuthey, A. L.; Wu, C. H.; Arighi, C. N.; Arminski, L.; Chen, C.; Chen, Y.; Garavelli, J. S.; Huang, H.; Laiho, K.; McGarvey, P.; Natale, D. A.; Ross, K.; Vinayaka, C. R.; Wang, Q.; Wang, Y.; Yeh, L. S.; Zhang, J.; *Nucleic Acids Res.* **2017**, *45*, D158. [Crossref]
34. Laskowski, R. A.; MacArthur, M. W.; Moss, D. S.; Thornton, J. M.; *J. Appl. Crystallogr.* **1993**, *26*, 283. [Crossref]
35. Laskowski, R. A.; *ProCheck*; University College London, UK, 1993.
36. Dolinsky, T. J.; Czodrowski, P.; Li, H.; Nielsen, J. E.; Jensen, J. H.; Klebe, G.; Baker, N. A.; *Nucleic Acids Res.* **2007**, *35*, W522. [Crossref]
37. Dolinsky, T. J.; Nielsen, J. E.; McCammon, J. A.; Baker, N. A.; *PDB2PQR* Server; Washington University, St. Louis, USA, 2004.
38. *ChemDraw Ultra*, version 12.0; PerkinElmer Informatics, USA, 2009.
39. *Avogadro*, version 1.2; The Open Chemistry Project, USA, 2012.

40. *GROMACS*, version 2019; The Gromacs Development Team, Sweden, 2019.
41. Hornak, V.; Abel, R.; Okur, A.; Strockbine, B.; Roitberg, A.; Simmerling, C.; *Proteins:Struct., Funct., Bioinf.* **2006**, *65*, 712. [Crossref]
42. Conev, A.; Rigo, M. M.; Devaurs, D.; Fonseca, A. F.; Kalavadwala, H.; de Freitas, M. V.; Clementi, C.; Zanatta, G.; Antunes, D. A.; Kavraki, L. E.; *Briefings Bioinf.* **2023**, *24*, 1. [Crossref]
43. Singh, R.; Ganeshpurkar, A.; Kumar, D.; Kumar, D.; Kumar, A.; Singh, S. K.; *J. Biomol. Struct. Dyn.* **2020**, *38*, 2533. [Crossref]
44. *AutoDock Vina*, version 1.2; The Scripps Research Institute, USA, 2010.
45. Brittain, M. K.; Brustovetsky, T.; Brittain, J. M.; Khanna, R.; Cummins, T. R.; Brustovetsky, N.; *Neuropharmacology* **2012**, *63*, 974. [Crossref]
46. Daina, A.; Michielin, O.; Zoete, V.; *Sci. Rep.* **2017**, *7*, 42717. [Crossref]
47. *SwissADME*; SIB Swiss Institute of Bioinformatics; Molecular Modelling Group, Switzerland, 2017.
48. Xiong, G.; Wu, Z.; Yi, J.; Fu, L.; Yang, Z.; Hsieh, C.; Yin, M.; Zeng, X.; Wu, C.; Lu, A.; Chen, X.; Hou, T.; Cao, D.; *Nucleic Acids Res.* **2021**, *49*, W5. [Crossref]
49. Xiong, G.; Wu, Z.; Yi, J.; Fu, L.; Yang, Z.; Hsieh, C.; Yin, M.; Zeng, X.; Wu, C.; Lu, A.; Chen, X.; Cao, D.; *ADMETlab 2.0*; Central South University, China, 2022.
50. Lipinski, C. A.; Lombardo, F.; Dominy, B. W.; Feeney, P. J.; *Adv. Drug Delivery Rev.* **1997**, *23*, 3. [Crossref]
51. Lipinski, C. A.; Lombardo, F.; Dominy, B. W.; Feeney, P. J.; *Adv. Drug Delivery Rev.* **2001**, *46*, 3. [Crossref]
52. Veber, D. F.; Johnson, S. R.; Cheng, H.-Y.; Smith, B. R.; Ward, K. W.; Kopple, K. D.; *J. Med. Chem.* **2002**, *45*, 2615. [Crossref]
53. Valdés-Tresanco, M. S.; Valdés-Tresanco, M. E.; Valiente, P. A.; Moreno, E.; *J. Chem. Theory Comput.* **2021**, *17*, 6281. [Crossref]
54. Kollman, P. A.; Massova, I.; Reyes, C.; Kuhn, B.; Huo, S.; Chong, L.; Lee, M.; Lee, T.; Duan, Y.; Wang, W.; Donini, O.; Cieplak, P.; Srinivasan, J.; Case, D. A.; Cheatham, T. E.; *Acc. Chem. Res.* **2000**, *33*, 889. [Crossref]
55. Xu, D.; Zhang, Y.; *Proteins:Struct., Funct., Bioinf.* **2013**, *81*, 229. [Crossref]
56. Martínez, L.; *PLoS One* **2015**, *10*, e0119264. [Crossref]
57. Wu, D.; Chen, Q.; Chen, X.; Han, F.; Chen, Z.; Wang, Y.; *Signal Transduction Targeted Ther.* **2023**, *8*, 217. [Crossref]
58. Wang, T.; Sun, J.; Zhao, Q.; *Comput. Biol. Med.* **2023**, *153*, 106464. [Crossref]
59. Andrade, R. J.; Chalasani, N.; Björnsson, E. S.; Suzuki, A.; Kullak-Ublick, G. A.; Watkins, P. B.; Devarbhavi, H.; Merz, M.; Lucena, M. I.; Kaplowitz, N.; Aithal, G. P.; *Nat. Rev. Dis. Primers* **2019**, *5*, 58. [Crossref]
60. Vijay, U.; Gupta, S.; Mathur, P.; Suravajhala, P.; Bhatnagar, P.; *Bio-Protoc.* **2018**, *8*, e2763. [Crossref]
61. Ahmed Juvale, I. I.; Abdul Hamid, A. A.; Abd Halim, K. B.; Che Has, A. T.; *Heliyon* **2022**, *8*, e09777. [Crossref]
62. O'Brien, F. E.; Dinan, T. G.; Griffin, B. T.; Cryan, J. F.; *Br. J. Pharmacol.* **2012**, *165*, 289. [Crossref]
63. Nishitoba, T.; Sato, H.; Oda, K.; Sakamura, S.; *Agric. Biol. Chem.* **1988**, *52*, 211. [Crossref]
64. Peng, X.; Liu, J.; Xia, J.; Wang, C.; Li, X.; Deng, Y.; Bao, N.; Zhang, Z.; Qiu, M.; *Phytochemistry* **2015**, *114*, 137. [Crossref]
65. Yang, L.; Kong, D.-X.; Xiao, N.; Ma, Q.-Y.; Xie, Q.-Y.; Guo, J.-C.; Ying Deng, C.; Ma, H.-X.; Hua, Y.; Dai, H.-F.; Zhao, Y.-X.; *Bioorg. Chem.* **2022**, *127*, 106025. [Crossref]
66. Wu, T. S.; Shi, L. S.; Kuo, S. C.; *J. Nat. Prod.* **2001**, *64*, 1121. [Crossref]
67. Liu, L. Y.; Yan, Z.; Kang, J.; Chen, R. Y.; Yu, D. Q.; *J. Asian Nat. Prod. Res.* **2017**, *19*, 847. [Crossref]
68. Liu, J.-Q.; Wang, C.-F.; Li, Y.; Luo, H.-R.; Qiu, M.-H.; *Planta Med.* **2012**, *78*, 368. [Crossref]
69. Poli, G.; Granchi, C.; Rizzolio, F.; Tuccinardi, T.; *Molecules* **2020**, *25*, 1971. [Crossref]
70. Segantine, A. S. A.; Gonçalves, A. S.; *Rev. Ifes Ciênc.* **2020**, *6*, 262. [Crossref]
71. Salmas, R. E.; Seeman, P.; Aksoydan, B.; Stein, M.; Yurtsever, M.; Durdagi, S.; *ACS Chem. Neurosci.* **2017**, *8*, 826. [Crossref]
72. Lei, T.; Hu, Z.; Ding, R.; Chen, J.; Li, S.; Zhang, F.; Pu, X.; Zhao, N.; *ACS Chem. Neurosci.* **2020**, *11*, 133. [Crossref]

Submitted: June 28, 2025
Final version online: September 17, 2025